Controlling gold nanoparticle assembly on electron beam-reduced nitrophenyl self-assembled monolayers *via* electron dose

Controlling gold nanoparticle assembly on electron beam-reduced nitrophenyl self-assembled monolayers *via* electron dose

Simon J. Leigh[1], Jose L. Prieto[2], James Bowen[3], Scott Lewis[4], Alex P.G. Robinson[3], Parvez Iqbal[1] and Jon A. Preece[1]*

[1]Nanoscale Chemistry Laboratory, School of Chemistry, The University of Birmingham, Edgbaston, Birmingham, B15 2TT, UK

[2]Instituto de Sistemas Optoelectrónicos y Microtecnología, Universidad Politécnica de Madrid, Ciudad Universitaria, Madrid, 28040, Spain

[3]School of Chemical Engineering, The University of Birmingham, Edgbaston, Birmingham, B15 2TT, UK

[4]School of Chemistry, The University of Manchester, Photon Science Institute, Oxford Rd, Manchester, M13 9PL, UK.

[*] To whom correspondence should be addressed

Abstract

Electron Beam Lithography is a well-established tool suitable for the modification of substrate surface chemistry. It therefore follows that the deposition and self-assembly of nanoparticles on a surface can be directed using this method. This work explores the effect of electron dose on the electron beam lithographic patterning of self-assembled monolayers (SAMs) on gold surfaces. Electron beam irradiation of the sample induces conversion of the SAM terminal functional aromatic nitro (NO_2) moieties to aromatic amino (NH_2) moieties. The cationic NH_2 functionalised regions direct the site-specific assembly of anionic citrate-passivated gold nanoparticles in aqueous solution at pH 4.5. Control of nanoparticle attachment to the SAM is demonstrated over the exposure range 5,000-125,000 μC/cm^2. Overexposure led to significant numbers of secondary electrons reaching the surface, causing conversion of functional aromatic moieties outside of the regions irradiated, which reduced feature quality and regional selectivity of adsorption.

Keywords Electron Beam Lithography, self-assembled monolayer, nanoparticle, citrate

1. Introduction

The use of bottom-up and top-down approaches to the formation of micro- and nano-structures is an area of increased research focus in recent years.[1-4] Within this field, the capability to direct and control the assembly of nanoparticles (NPs) into distinct patterns and arrays on a variety of substrates is seen as process step critical to the fabrication of next-generation electronic devices[5] and sensors.[6] In particular, the drive to use ultrathin molecular films as pseudo-resist systems that can be lithographically patterned to exhibit selectivity in the attachment of NPs on metal,[7] semiconductor,[8] and insulator surfaces[9] has seen a number of significant research efforts. The main methodology employed has been to lithographically alter the characteristics of 2D self-assembled monolayers (SAMs) of organic molecules covalently bound to a planar substrate.[10] The immobilization of NPs on these monolayers is achieved through mechanisms such as hydrogen bonding[11] or electrostatic attraction[12] between organic ligands on the exterior of the NPs and regions of differing chemical functionality induced in the SAM *via* lithographic patterning. Such a combination of techniques has been termed 'precision chemical engineering'.[13] The lithographic step can be achieved using a number of different processes, such as UV photolithography, electron beam lithography, scanning probe microscopy and microcontact printing.[14-17] The modification of the chemical functionality of the SAM can be achieved a number of ways, through the energetic desorption and subsequent replacement of molecules, the mechanical desorption of molecules, the microcontact printing of a molecular template and energetically induced chemical reactions.[18-21] However the step is achieved, a number of the processes result in either an off or on preference for nanoparticle attachment, meaning fine control over the surface density of nanoparticles cannot be achieved. It has previously been reported by ourselves and other groups that EBL and X-ray irradiation can induce chemical changes on surfaces such as the reduction of the aromatic NO_2 group of a SAM to that of an NH_2 group.[13, 22-25] Grunze *et al.*[22-25] first demonstrated the EBL induced reduction by exposing a SAM of 4'-nitro-1,1'-biphenyl-4-thiol on a Au surface. The periphery NO_2 moieties were converted to the respective NH_2 moieties allowing generation of 1 µm down to 10 nm wide lines. FTIR studies revealed a more rigid structure in the exposed regions compared to the unexposed areas. From these observations, it was proposed that dehydrogenation of the phenyl rings had occurred, with subsequent cross-linking between the phenyl rings, with the released hydrogen involved in the NO_2 to NH_2 conversion.[26] Further investigation has revealed the need to include a phenyl ring within the SAM molecular structure to achieve the desired NO_2 to NH_2 reduction.[27-28]

Using an aromatic-NO_2 terminated SAM of 6-(4-nitrophenoxy) hexane-1-thiol (NPHT), in this work it is shown that by varying the dose of electrons used during the EBL process, the surface density of attached citrate stabilized Au nanoparticles (AuNPs) can be influenced, with the dose versus response behaviour mimicking that of a conventional photoresist. The affinity of the Au-NPs for protonated NH_2 terminated surfaces[23,29] can be viewed as an assay for the effectiveness of the reduction process. Controlling the surface assembly of metal nanoparticles is an area of key interest as they have shown potential applications in the areas of electronics,[30,31] photonics[32] and sensors.[33] We further show that when considering implementing this dose related control, critical parameters such as inter-feature spacing and nanoparticle concentration are also seen to influence nanoparticle attachment. High electron doses are also shown to cause pattern inversion which can be used to overcome feature broadening effects in order to improve feature resolution. Analysis of attached nanoparticle density, features and surface chemical modification is carried out using a combination of scanning electron microscopy (SEM), atomic force microscopy (AFM) and AFM adhesion force mapping.

2. Materials and Methods

2.1 Materials

The commercially available chemicals 4-nitrophenol, 1,6-dibromohexane and $HAuCl_4.3H_2O$ were purchased from Sigma-Aldrich and used as received. Solvents and other chemicals were purchased from Fisher Scientific (DCM, EtOAc, Et_2O, MeOH and HCl) or Sigma-Aldrich (anhydrous EtOH). Thin-layer chromatography (TLC) was carried out on aluminium plates coated with silica gel 60 F254 (Merck 5554). TLC plates were air-dried and analysed under a short wave UV lamp (254 nm). Column chromatographic separations were performed on silica gel 120 (ICN Chrom 32-63, 60 Å).

2.2 Synthesis of 1-(6-bromo-hexyloxy)-4-nitro-benzene (2)

The synthetic procedure for NPHT was followed as per the synthetic procedure described previously [18]. A suspension of K_2CO_3 (5.45 g, 39.49 mmol) in a solution of **1** (2.74 g, 19.73 mmol), 1, 6-dibromohexane (9.63 g, 39.47 mmol) in MeCN (150 mL) was heated under reflux for 24 h with a $CaCl_2$ guard. The reaction mixture was allowed to cool to room temperature and concentrated *in vacuo* (20 mL). Water (100 mL) was added and the aqueous layer was extracted with EtOAc (3 x 50 mL). The combined organic layers were washed with brine (20 mL), dried ($MgSO_4$), filtered and the solvent removed *in vacuo,* yielding a white solid as the crude product. The solid was absorbed onto silica and purified *via* silica gel column chromatography (graded elution: 0 to 30 % EtOAc in hexane, increments of 5% per 100 mL of eluent used). The solvent was removed *in vacuo* to yield a yellow oil (4.65 g, 76 %).

^{1}H NMR (300 MHz, $CDCl_3$): 8.19 (d, *J* = 9.20 Hz, 2H), 6.93 (d, *J* = 9.20 Hz, 2H), 4.05 (t, *J* = 6.44 Hz, 2H, $OC\underline{H}_2C_5H_{10}Br$), 3.43 (t, *J* = 6.62 Hz, 2H, $OC_5H_{10}C\underline{H}_2Br$), 1.92-1.82 (m, 4H, $OC_6\underline{H}_{12}Br$), 1.54-1.50 (m, 4H, $OC_6\underline{H}_{12}Br$); ^{13}C NMR (75 MHz, $CDCl_3$): δ_C 160.5, 137.3, 124.9, 113.4, 67.6, 32.6, 31.5, 27.8, 26.8, 24.1; λ_{max}/cm^{-1} (film): 2939s, 2860s, 1607s, 1593s, 1512s; m/z (ESMS): 302 ([M + Na]$^+$, 100 %), 304 ([M + Na], 90 %); m/z (HRMS): calc. 302.0392 for $C_{12}H_{17}NO_3Br$, found 302.0389.

2.3 Synthesis of 6-(4-nitrophenoxy) hexane-1-thiol (NPHT, 3)

A solution of **2** (0.96 g, 3.18 mmol) and thiourea (0.27 g, 3.50 mmol) in anhydrous EtOH (40 mL) was heated under reflux and N_2 atmosphere for 20 h. 5 M NaOH (0.64 mL, 3.18 mmol) was added and the reaction mixture further heated under reflux for 4 h. The mixture was allowed to cool to room temperature and concentrated *in vacuo* (20 mL). Water (50 mL) was added and acidified with 2M HCl to yield a white precipitate. The aqueous layer was extracted with further additions of DCM (4 x 50 mL). The combined organic layers were dried ($MgSO_4$), filtered, and solvent removed *in vacuo* to yield a yellow oil as the crude product. The crude product was dissolved in minimum amount of DCM and absorbed onto silica followed by purification *via* flash silica gel column chromatography (graded elution: 0 to 30% EtOAc in hexane, increase increments of 5% per 100 mL of eluent used). The solvent was removed *in vacuo* to yield a yellow oil (0.62 g, 76%).

^{1}H NMR (300 MHz, $CDCl_3$): 8.19 (d, *J* = 9.20 Hz, 2H, $\underline{H}$-2), 6.93 (d, *J* = 9.20 Hz, 2H, $\underline{H}$-3)), 4.04 (t, *J* = 6.44 Hz, 2H, $OC\underline{H}_2C_5H_{10}SH$), 2.54 (q, *J* = 7.72 Hz, 2H, $OC_5H_{10}C\underline{H}_2SH$), 1.85-1.80 (m, 2H, $OCH_2C\underline{H}_2C_4H_8SH$), 1.67-1.63 (m, 2H, $OC_4H_8C\underline{H}_2CH_2SH$), 1.49-1.47 (m, 4H, $OC_2H_4C_2\underline{H}_4C_2H_4SH$), 1.34 (t, *J* = 7.72 Hz, 1H, $S\underline{H}$); ^{13}C NMR (75 MHz, $CDCl_3$): δ_C 161.8, 138.8, 126.3, 114.7, 69.0, 34.1, 29.2, 28.3, 25.8, 24.8 (all $OC_6H_{12}SH$); λ_{max}/cm^{-1} (film): 2994m, 2856m, 1606s, 1592s, 1510s; m/z (ESMS): 278 ([M + Na]$^+$, 100 %); m/z (HRMS): calc. mass for $C_{12}H_{17}NO_3S$ 278.0827, found 278.0832; elemental analysis for $C_{12}H_{17}NO_3S$ requires C, 56.45%; H, 6.71%; N, 5.49%, found C, 56.55%; H, 6.84%; N, 5.24%.

2.4 Preparation of the Au substrates

Au substrates were prepared using an Auto 306 vacuum evaporation chamber (Edwards) in a two pump system; the pressure was reduced to ~10^{-7} bar followed by a subsequent reduction to ~10^{-10} bar on the glass microscope slides. Prior to the evaporation of Au onto the glass slides, a Cr layer (6 nm) was evaporated onto the glass slides by heating Cr pieces (Agar Scientific, 99.99 % purity) of ~ 5 mm^3 volume by electrical resistance using a voltage of 30 V and a current of 3 A, to promote adhesion of the Au to the base material. Au was deposited in a similar manner. An Au wire (Advent Research Materials, 99.99+ % purity) of 0.5 mm diameter, which was placed into a Mo boat (Agar Scientific) was heated. The Au wire was heated by electrical resistance using a voltage of 10 V and a current of 3 A until ~ 100

nm of Au had been deposited onto the desired surface within the vacuum evaporation chamber. Deposition rates were monitored using a quartz crystal microbalance (QCM) thickness monitor. A deposition rate between 0.05- 0.1 nm/s was used for both Cr and Au layers. The Au substrates were cut to 1 x 1 cm^2 using a diamond tipped scriber.

2.5 Preparation of the SAMs

Prior to the preparation of the SAMs, the glassware and the Au substrates were cleaned thoroughly to remove contaminants. Initially, the glassware was immersed in piranha solution (conc. H_2SO_4:30 % H_2O_2 = 7:3) for 60 min followed by extensive rinsing with Ultra High Purity (UHP) H_2O (Resistivity = 18 MΩ.cm). The following steps were subsequently followed: 30 min sonication in UHP H_2O, dried in oven at 120 °C for 30 min, allowed to cool to room temperature, 30 min sonication in EtOH, oven dried at 120 °C for 30 min and wrapped in Al foil before use to prevent exposure to airborne contaminates and used within 24 h. The Au substrates were immersed in piranha solution at room temperature for 10 min with occasional stirring. Followed by thorough rinsing with UHP H_2O, then with EtOH (HPLC grade) and immediately immersed in a 1 mM solution of NPHT in EtOH (HPLC) for 24 hours. Finally, the SAMs were rinsed thoroughly with EtOH (HPLC grade) and dried with a stream of N_2.

2.6 SAM characterisation

2.6.1 Ellipsometry

The thicknesses of the deposited monolayers were determined by spectroscopic ellipsometry. An Horiba Jobin-Yvon UVISEL ellipsometer with a Xe light source was used for the measurements. The angle of incidence was fixed at 70^o. A wavelength range of 280-820 nm was used. DeltaPsi software was employed to determine the thickness values and the calculations were based on a three-phase ambient/SAM/Au model, in which the SAM was assumed to be isotropic and assigned a refractive index of 1.50. The thicknesses reported are the average of six measurements taken on each SAM.

2.6.2 Water contact angle

Contact angles were determined by the sessile drop method using a home built contact angle apparatus, equipped with a charged coupled device (CCD) camera that is attached to a personal computer for video capture. The advancing (θ_a) and receding (θ_r) contact angles were measured as liquid was added quasi-statically or removed from the drop by a micro syringe. The drop is shown as a live video image on the PC screen and digitally recorded. The acquisition rate was 4 frames per second. Stored images of the droplets were analysed with software from FTÅ. Contact angles were determined from an average of five different measurements on each sample.

2.6.3 X-ray photoelectron spectroscopy (XPS)

Elemental composition of the SAMs were analysed using an Escalab 250 system (Thermo VG Scientific) operating with Avantage v1.85 software under pressure of ~ 5 x 10^{-12} bar. An Al K_α X-ray source was used, which provided a monochromatic X-ray beam with incident energy of 1486.68 eV and circular spot size of ~0.2 mm^2 was employed. The samples were attached onto a stainless steel holder using double-sided carbon adhesive tape (Agar Scientific, UK). In order to minimise charge retention on the sample, the samples were clipped onto the holder using stainless steel or Cu clips. The clips provided a link between the sample and the sample holder for electrons to flow, which the glass substrate inhibits. Low resolution survey spectra were obtained using a pass energy of 150 eV over a binding energy range of -10 eV to 1200 eV obtained using 1 eV increments. The spectra recorded were an average of 3 scans. The high-resolution spectra were obtained using a pass energy of 20 eV and 0.1 eV increments over a binding energy range of 20-30 eV, centred on the binding energy of the electron environment being studied. A dwell time of 20 ms was employed between each binding energy increment.

2.6.4 Atomic Force Microscopy (AFM)

AFM topography imaging was carried out using a Dimension D3100 AFM (Digital Instruments, Santa Barbara, USA) in tapping mode using etched silicon probes. Force mapping measurements were carried out in contact mode (NanoWizard II, JPK Instruments, Berlin, Germany). Nominal cantilever spring constants were used throughout.

2.7 Synthesis of citrate stabilised Au nanoparticles (Au-NPs)

Citrate-stabilised Au nanoparticles (Au-NPs) were synthesised *via* the Frens method.[34] Briefly, an aqueous solution of $HAuCl_4.3H_2O$ (9.9 mg, 100 mL) was heated under reflux for 5-10 min. An aqueous solution of sodium citrate (22.8 mg, 2 mL) was added. Heating under reflux was continued for a further 10 min to ensure complete reduction of the Au salt. The red colloidal solution was centrifuged three times for 10 min (3,500 rpm) and the supernatant collected. Adjustment of the colloid pH to 4.5 was carried out using HCl (0.06 M)

2.8 Synthesis of concentrated citrate stabilised Au nanoparticles (C-Au-NPs)

A concentrated solution of citrate-stabilised Au nanoparticles (C-Au-NPs) was also synthesised *via* the Frens method.[45] An aqueous solution of $HAuCl_4.3H_2O$ (40 mg, 49mL) was heated under reflux for 5-10 min. An aqueous solution of sodium citrate (80 mg, 1 mL) was added. Heating under reflux was continued for a further 5 min to ensure complete reduction of the Au salt. The colloidal solution was left to cool while stirring for 1 hour. Finally, the dark red solution was centrifuged three times for 10 min (3,500 rpm) and the supernatant collected. Adjustment of the colloid pH to 4.5 was carried out using HCl (0.06 M)

2.9 Pattern fabrication

2.9.1 Electron beam lithography (EBL)

Electron Beam Lithography was carried out using a dedicated Electron Beam Lithography instrument (Crestec CABL-9500C High Resolution Electron Beam Lithography System - ISOM, Madrid). The beam voltage was kept constant at 50 keV with a current of 5 nA. The beam current was checked before and after lithographic processing using a Faraday cup. The beam diameter was kept constant at 10 nm and samples were secured to the sample stage with conductive tape to ground the samples.

2.9.2 Attachment of Au-NPs and C-Au-NPs

After electron beam exposure, substrates were immersed in an aqueous solution of citrate stabilised Au nanoparticles (5 mL) for 2 hours at pH 4.5.[15] After immersion, substrates were rinsed with UHP H_2O, and dried under a stream of N_2. Samples were subsequently examined using SEM and AFM.

2.10 Monte Carlo Simulation

Monte Carlo simulations of the electron scattering in this system were run. The structure that was modeled here was 1.4 nm of 6-(4-nitrophenoxy)hexane-1-thiol on 100 nm Au on 6 nm Cr on a Si substrate. The physical properties of each material are given in Table 1.

Table 1: Physical properties of the materials used in the Monte Carlo model

Physical property	SAM	Au	Cr	Si
Density (g/cm^3)	4.09	79	24	2.33
Atomic Number	254.325	196.967	51.99	14
Atomic Weight (g/mol)	0.86309	19.3	7.19	28.0855
Ionization Potential (eV)	0.084	0.79	0.257	174 [45]

The simulated exposure parameters were a step size of 6.104 nm, acceleration voltage of 50 keV, and a current of 5 nA. To achieve an exposure dose of 30,000 μC/cm^2, 70,000 electrons were used. Table 2 shows the number of electrons used for each exposure dose. For each dose the simulation was run 200,000 times to reduce statistical error.

Table 2: The number of electrons that were calculated for each exposure dose.		
Dose (μC/cm^2)	Dwell time (μs)	Number of electrons
30,000	2.231	70,000
40,000	2.981	93,000
50,000	3.726	116,000
60,000	4.471	140,000
70,000	5.216	163,000
80,000	5.961	186,200
90,000	6.707	209,500

3. Results and discussion

A schematic representation of the experimental steps carried out is detailed in Fig. 1. Step 1 is the formation of the NPHT SAM on Au surfaces. Step 2 is the patterning of large-scale features using EBL and subsequent immersion in Au-NP solution. Step 3 is the patterning of linear features on the NPHT SAM and immersion in Au-NP solution, and finally step 4 is the patterning of linear features at high electron doses and subsequent attachment of Au-NPs from a concentrated Au-NP solution.

3.1 SAM characterisation

The NPHT SAMs showed ellipsometric thicknesses (1.36 $\pm$ 0.19 nm) in good agreement with the estimated value (1.5 nm, Chem3D Software, Cambridgesoft, UK), taking into account the characteristic tilt angle of SAMs of this type.[35] Water contact angles of NPHT SAMs (θ_a = 67 $\pm$ 1^o, θ_r = 45 $\pm$ 1^o) also agreed with literature values (θ_a = 64^o) for aromatic-NO_2 terminated SAMs on Au surfaces.[35] The elemental composition of the monolayers was determined by XPS. The elements C, N, O, S and Au were monitored in the spectra. The XPS survey spectrum confirmed the presence of peaks at binding energies; 286, 400, 531 and 162 eV which are indicative of the presence of C 1s, N 1s, O 1s and S $2p_{3/2}$ photoelectrons, respectively.[36]

3.2 SAM sensitivity to electron dose

To assess the effect of electron dosage on the reduction of the surface tethered NO_2 group of NPHT to NH_2 groups, a grid pattern of 120 µm x 120 µm squares, spaced 200 µm apart, was exposed at a beam energy of 50 keV to a range of increasing electron dosages (5,000 – 125,000 µC/cm^2). The total fabrication time for the grid was approximately 14 h. After exposure, the sample was imaged at low beam energy utilising the SEM capabilities of the EBL instrument (Fig. 2a) and subsequently immersed into a solution of Au-NPs. After the immersion into Au-NPs the sample was re-imaged with SEM, (Fig. 2b).

A clear contrast in appearance is seen between the surfaces before (Fig. 2a) and after immersion (Fig. 2b) in the Au-NP solution. After the immersion, the image contrast between the exposed regions and surrounding SAM is much brighter, indicative of Au-NPs being adsorbed to the electron exposed region. It should be noted that although in Fig. 2a all the squares appear to have similar contrast with respect to the surrounding regions, they were fabricated at increasing electron dosages, with the bottom-left square of image B fabricated at a dose of 5,000 µC/cm^2 and then increasing in increments of 5,000 µC/cm^2 left to right and increasing bottom to top. The highlighted regions 1 and 2 correspond to electron doses of 40,000 and 70,000 µC/cm^2 respectively. The gradient in the observed contrast is clearly seen in Fig. 2b, after immersion in Au-NPs, with the bottom left square (5,000 µC/cm^2) showing a low contrast, indicative of a low degree of Au-NP attachment. Over the range of doses, the optimum feature fidelity appears to occur over the range of 25,000 to 45,000 µC/cm^2. At doses greater than 45,000 µC/cm^2 there is a gradual loss in edge resolution, leading to characteristic shadowing effects normally observed after high dose EBL.[30] The inset magnified sections of the SEM images (Fig. 2b, position 2) confirms this loss of edge resolution which is not as pronounced before Au-NP attachment.

The number of nanoparticles attached on each region per unit area were counted and the corresponding graph of nanoparticle attachment is presented in Fig. 2d. From this graph it is possible to observe that the maximum number of nanoparticles attach to the surface at a dose of 30,000 µC/cm^2. From this value we can infer that this is the optimal dosage required for the conversion of the NO_2 group to an NH_2 group for features of this size. The shape of the EBL electron dose versus nanoparticle adsorption graph mimics that of the response of a conventional negative polymeric EBL resist to increasing electron dose, where exposure at a certain critical electron dose leads to a rapid change in the retained film thickness and higher doses can lead to a decrease in the retained film thickness.[28, 37-38] At electron doses above those affording maximum nanoparticle attachment, the amount of nanoparticle attachment decreases, possibly indicating degradation of the SAM due to the increased amount of secondary electrons that are produced, as discussed below.

The rationale for the attachment of the Au-NPs is that the surface NO_2 groups of the NPHT become reduced upon electron beam exposure and are converted to NH_2 groups. It is believed that the reduction of the NO_2 group to an NH_2 group is carried out not by the primary incident electrons, but by secondary low energy electrons emitted from the surface.[16, 23] The NH_2 groups, when immersed in the acidic Au-NP (pH 4.5) solution become protonated, forming NH_3^+ groups, which are able to bind electrostatically to the anionic, citrate-stabilised (COO^-) Au-NPs. The effect of increasing the primary electron dose is to increase the number of lower energy secondary electrons generated within the SAM and backscattered from the substrate into the SAM. At high beam energies with Au substrates, these backscattered electrons will potentially be distributed over a range of tens of microns from the primary exposure point.

The optimal electron dose of 30,000 $\mu C/cm^2$ is comparable to the dose of 35,000 $\mu C/cm^2$ required to carry out the large-scale nitro reduction on a biphenyl based NO_2 terminated SAM on gold.[25] Similar experiments to those presented here have shown that EBL with subsequent attachment of Au nanoparticles can be seen with an analogous SAM on SiO_2.[23] However, the electron dose required for the patterning on SiO_2 is much lower than required for a SAM on Au and it is believed that the difference in EBL behaviour between SAMs on Au and Si is related to the differing film thicknesses and electron scattering characteristics of the two underlying surfaces.[16, 39]

3.3 AFM adhesion force mapping of EBL exposed samples

In order to visualise the modification in surface chemistry caused by the EBL process, AFM adhesion force mapping was carried out to gain insight into the adhesive response of the SAM samples after electron exposure, but before immersion in Au-NPs. A more complete discussion of the principles behind adhesion force mapping has been reported by Noy.[40] Adhesion force mapping was chosen as this is generally considered a non-destructive characterisation technique. Furthermore, SAMs of this type have previously been shown to be sensitive to prolonged exposure to X-rays, making XPS unsuitable for this task. Adhesion force information is collected from the retraction portion of the force curve in the 'snap-off' region. These forces are a combination of several forces, however in ambient conditions in air capillary forces on the order of 10-100nN dominate.

Operating the AFM in force mapping mode with a pyramidal imaging AFM tip over the boundary between an exposed and unexposed region (at 40,000 $\mu C/cm^2$) revealed a gradient contrast between the two regions on both the approach and retraction of the AFM tip to/from the sample surface (Fig. 3a). The pyramidal tip was then used to carry out height analysis of the same region and revealed no corresponding gradient in the height profile. After determination of the deflection sensitivity of the cantilever and calibration of the spring constant, the average adhesive force upon tip retraction of each region was calculated. The NH_2 terminated regions exhibited an adhesive force of approximately 120 nN (Fig. 3a, upper region). This value is lower than the previously reported literature values for NH_2 terminated SAMs on Au surfaces (340 nN), however this can be rationalized firstly due to the use of standard pyramidal probe instead of a dedicated force mapping probe,[41] and more significantly by the fact that the NO_2 to NH_2 conversion potentially does not yield a fully converted SAM at the analysed electron dose. The NO_2 terminated regions of the sample exhibited an adhesive force of approximately 40 nN, a lower value than for the NH_2 regions and rationalised by the reduced interaction of the NO_2 group with the SiO_2 surface of the tip.

3.4 Effect of electron dose on the patterning of linear features

In order to assess whether the electron dose used for patterning of the large-scale features would be appropriate for linear features or tracks, fabrication of linear features on NPHT SAMs on Au was carried out. Grids of lines of 500 nm width with a 400 nm gap (Type A) and 250 nm wide lines with a 550 nm gap (Type B) were exposed over a smaller range of electron doses (30,000 to 45,000 $\mu C/cm^2$) which previously afforded a high degree of Au-NP attachment and feature fidelity. The sample was then immersed in Au-NPs (pH 4.5).

Fig. 4a and the inset magnified image shows a grid of type A lines exposed at 40,000 $\mu C/cm^2$. In agreement with the previous experiment, there was a high degree of nanoparticle attachment and the lines were clearly visible. Fig. 4b

presents an SEM image of a type B at the same electron dose. In contrast, the attachment of nanoparticles on these features is significantly less, with the majority of the nanoparticles attaching at what appears to be the edge of the features. Analysis of the width of both the type A and type B features after immersion in Au-NPs showed that the width of the lines was broader than that written by the electron beam. This broadening increased with electron dose, so therefore appears to be resultant from scattering and secondary effects after electron exposure. Type A features broadened by up to 60 % at a dose of 45,000 $\mu C/cm^2$. Type B features followed the same dose-related feature broadening pattern, but with only a small amount of nanoparticle attachment presumably as a result of a larger gap and narrower feature combination to give fewer back scattered and secondary electrons impinging on adjacent features.

As features at a dose of 45,000 $\mu C/cm^2$ had broadened by 60 %, it was necessary to define type C features where the line spacing was 1,000 nm and the feature width maintained at 250 nm in order to avoid merging of features. Interestingly, this spacing increase resulted in no nanoparticle attachment on the EBL patterned features. The lack of nanoparticle attachment on type C features is an indicator that the proximity of adjacent features may be a significant controlling factor in feature quality and is supported by the observation in Fig. 4b where only the periphery of the features exhibits particle adsorption. In an ultra thin SAM resist, many secondary electrons result from backscattering of the primary electrons from the underlying substrate that expose outside the focus of the primary electron beam as the SAM is too thin to engender much forward scattering. These backscattered electrons (BE) can scatter over large distances (up to tens of microns) within the sample and the subsequent secondary electron collisions result in further scattering and exposure effects in adjacent features at the surface. The inter-feature spacing controlled attachment of Au-NPs further agrees with the theory that scattered electrons play a key part in the SAM reduction process.[43] Thus the lack of nanoparticle attachment on the features with increased spacing is due to secondary electrons spreading within the inter-feature gap and not only within the features themselves,[34] leading to conversion of the NO_2 groups in a complex fashion dependent upon feature spacing and dose. This inter-feature spacing controlled attachment of nanoparticles, demonstrates that EBL feature quality on SAM surfaces is not purely controlled by the electron dose. In order to effectively use EBL to pattern SAMs, careful consideration of the feature size and spacing to be used is thus required due the increased reliance on backscattering of electrons due to the ultrathin nature of the films used.

3.5 Immersion of 1,000 nm spaced features in concentrated citrate-stabilised Au nanoparticles (C-Au-NPs)

It was believed that the lack of nanoparticle attachment on the 1000 nm spaced features was a function of a change in the kinetics of absorption due to the less efficient reduction of NO_2 to NH_2 in the feature regions. In order to try and visualise any remnant surface patterning, a concentrated (~4x) solution of Au-NPs (C-Au-NPs) was used to immerse the type C features. After immersion in the C-Au-NP solution, attachment of nanoparticles had occurred within the type C exposed features. It is believed that use of the concentrated solution of nanoparticles is able to overcome the lesser degree of conversion of the NO_2 to NH_2 groups. The linewidths of the type C linear features after immersion in C-Au-NPs were examined with AFM (Fig. 5a). AFM images showed that the features sizes varied from the intended feature sizes, with increasing feature broadening as a function of increasing electron dosage as seen earlier (Fig. 5a, Region I). The 250 nm features were seen to broaden with increased electron dose. There was also increased absorption of the nanoparticles in the gaps between features, which also increased with electron dose (Fig. 5b and *inset*). It is believed that the C-Au-NPs are not only able to overcome the reduction in conversion of the NO_2 to NH_2 groups but also able to aid in visualising the increasing background dose due to scattering that occurs between the exposed features.

3.6 Pattern inversion at high electron doses

For the type C features at doses of 80,000 $\mu C/cm^2$ and above it was observed that pattern inversion behaviour occurred after substrate immersion in the C-Au-NP solution. No attachment of C-Au-NPs was observed in the planned EBL exposed areas, but a high degree of attachment was seen in the intervening gaps (Fig. 5c). This inversion behaviour is believed to be attributable to the larger overall dose of electrons causing damage to the SAM structure

as seen by Toikkanen *et al*.[42] with NO_2 to NH_2 conversion occurring in the gaps between features. This behaviour agrees with the hypothesis that at increasing electron doses on closely nested features, there is an interplay between, causing the chemical conversion to afford nanoparticle attachment, feature broadening and degradation of the SAM structure.

AFM imaging also confirmed the pattern inversion behaviour seen with SEM, with feature sizes becoming less broadened by scattering effects (Fig. 5a, Region B), yet inverted in attachment of nanoparticles. This increase in feature resolution for inverted patterns could be a key step in overcoming the apparent loss in resolution due to scattering effects in EBL using ultrathin resists on gold, allowing for better defined nanostructures to be created by deposition of a secondary species within the gaps between nanoparticle tracks or on top of the nanoparticle tracks. However, such a fabrication method is reliant upon forming nested features and hence may not be practical for single, isolated features. Further work is required to understand whether this effect can be accurately controlled through interplay of electron dose, beam energy, feature size and spacing and nanoparticle concentration.

3.7 Monte Carlo Simulations

The Monte Carlo simulation used is fully described elsewhere[43]. Fig. 6 shows the scattering trajectories of incident electrons that experience a number of collisions with the atoms in the sample. It shows the interaction when the doses of 30,000 to 90,000 $\mu C/cm^2$ are used. In all cases, the electrons diverge away from the incident beam. It was observed from Fig. 6(g) that the sample experiences significant scattering in to the unexposed areas in comparison to the sample shown in Fig. 6(a) It can be seen that when the dose is increased above 60,000 $\mu C/cm^2$, the sample experiences an increasing number of electrons scattered at angles larger than 80˚ (indicated in blue)[44] and this is evident in Fig. 6. These electrons in turn are back scattered into the SAM exposing it from underneath. The number of low energy back scattered electrons, averaged over the simulation area, and incident into the SAM is shown as a function of dose in Fig. 7. The number of back scattered electrons generated in a gold film is inversely proportional to the exposure energy (~ 0.05 for a 100 nm Au film and 50 keV electrons, and ~0.25 at 20 keV), suggesting that sensitivity could be drastically increased at lower exposure energy.[45]

4. Conclusions

We have presented a characterisation of the electron dosages required to carry out spatially selective modification of NO_2 terminated thiol SAMs on Au surfaces. If inter-feature distances are too large, then deposition of nanoparticles may not occur, due to incomplete conversion of SAM surface chemistry as the number of backscattered and secondary electron contributions from neighbouring features are reduced. It has also been demonstrated that deposition of colloids on EBL fabricated patterns on SAMs is a highly complicated system with many factors such as electron dose, feature size, proximity effects and the colloid solution itself playing a key role in the resolution and type of features achievable. The quality and type of fabricated features can be varied by careful choice of electron dose during the EBL stage of the fabrication process, allowing for both positive and negative pattern formation. Consideration of the type of features required is needed, as the doses required for nested features will differ to the doses required for isolated features. The use of an EBL modified SAM and attachment of Au colloids can overcome the limitations of pattern transfer processes associated with current resist based systems, by precisely controlling the deposition of nanometer-scale species, which can serve as a template for further nanostructure fabrication. Further work is required to fully characterise and understand all the mechanisms at play during the fabrication procedure and understand the key NO_2 to NH_2 conversion threshold required to template the attachment of nanoparticles. Beyond this, the move will be to discover whether any of these factors can be leveraged to better control and direct the deposition of a range of other nanoscale species.

Acknowledgements
This work was supported by EU grant (Nano3D STRP 014006), research visit to CT-ISOM from the Spanish "Ministerio de Ciencia e Innovación for SJL, EU Postdoctoral Fellowship for PI. The JPK NanoWizard II AFM used in this research was obtained through Birmingham Science City: Innovative Uses for Advanced Materials in the Modern World (West Midlands Centre for Advanced Materials Project 2), with support from Advantage West Midlands (AWM) and part funded by the European Regional Development Fund (ERDF).

References

1. H. Wagner, Y. Li, M. Hirtz, L. Chi, H. Fuchs, A. Studer, Site specific protein immobilization into structured polymer brushes prepared by AFM lithography, Soft Matter 7 (2011) 9854-9858.
2. B. Gao, G.H. Bernstein, M. Lieberman, Self-assembled monolayers of poly(ethylene glycol) siloxane as a resist for ultrahigh-resolution electron beam lithography on silicon oxide, J. Vac. Sci. Technol. B 27 (2009) 2292-2300.
3. M. Hirtz, M.K. Brinks, S. Miele, A. Studer, H. Fuchs, L. Chi, Structured polymer brushes by AFM lithography, Small 5 (2009) 919–923.
4. Z. Xie, X. Zhou, X. Tao, Z. Zheng, Polymer nanostructures made by scanning probe lithography: recent progress in material applications, Macromol. Rapid Commun. 33 (2012) 359–373.
5. G. Schmid, U. Simon, Gold nanoparticles: assembly and electrical properties in 1-3 dimensions, Chem. Commun. 6 (2005) 697-710.
6. S. Liu, Z. Tang, Nanoparticle assemblies for biological and chemical sensing, J. Mater. Chem. 20 (2010) 24-35.
7. J.C. Love, L.A. Estroff, J.K. Kriebel, R.G. Nuzzo, G.M. Whitesides, Self-assembled monolayers of thiolates on metals as a form of nanotechnology, Chem. Rev. 105 (2005) 1103-1170.
8. L.C.P.M. deSmet, H. Zuilhof, E.J.R. Sudholter, L.H. Lie, A. Houlton, B.R. Horrocks, Mechanism of the hydrosilylation reaction of alkenes at porous silicon: Experimental and computational deuterium labeling studies, J. Phys. Chem. B 109 (2005) 12020-12031.
9. P.E. Laibinis, G.M. Whitesides, ω-Terminated alkanethiolate monolayers on surfaces of copper, silver, and gold have similar wettabilities, J. Am. Chem. Soc. 114 (1992) 9022-9028.
10. H. Sugimura, K. Hayashi, Y. Amano, O. Takai, A. Hozumi, Friction force microscopy study on photodegradation of organosilane self-assembled monolayers irradiated with a vacuum ultraviolet light at 172 nm, J. Vac. Sci. Technol. A 19 (2001) 1261-1265.
11. R. Zirbs, F. Kienberger, P. Hinterdorfer, W.H. Binder, Directed assembly of Au nanoparticles onto planar surfaces via multiple hydrogen bonds, Langmuir 21 (2005) 8414-8421.
12. P. Iqbal, K. Critchley, J. Bowen, D. Attwood, D. Tunnicliffe, S.D. Evans, J.A. Preece, Fabrication of a nanoparticle gradient substrate by thermochemical manipulation of an ester functionalized SAM, J. Mater. Chem. 17 (2007) 5097-5110.
13. P.M. Mendes, J.A. Preece, Precision chemical engineering: integrating nanolithography and nanoassembly, Curr. Op. Coll. Surf. Sci. 9 (2004) 236-248.
14. J.M. Calvert, J.H. Georger, J.M. Schnur, P.E. Schoen, M.C. Peckerar, P.E. Pehrsson, Deep UV photochemistry and patterning of self-assembled monolayer films, Thin Solid Films 210-211 (1992) 359-363.
15. N. Ballav, S. Schilp, M. Zharnikov, Electron-beam chemical lithography with aliphatic self-assembled monolayers, Angew. Chem. Int. Ed. 47 (2008) 1421–1424.
16. J. Hyun, J. Kim, S.L. Craig, A. Chilkoti, Enzymatic nanolithography of a self-assembled oligonucleotide monolayer on gold, JACS 126 (2004) 4770-4771.
17. K.I. McConnell, J.H. Slater, A. Han, J.L. West, J. Suh, Microcontact printing for co-patterning cells and viruses for spatially controlled substrate-mediated gene delivery, Soft Matter 7 (2011) 4993-5001.
18. J. Zhao, A. Terfort, M. Zharnikov, Gold nanoparticle patterning on monomolecular chemical templates fabricated by irradiation-promoted exchange reaction, J. Phys. Chem. C. 115 (2011) 14058-14066.
19. J-F. Liu, J.R. von Ehr, C. Baur, R. Stallcup, J. Randall, K. Bray, Fabrication of high-density nanostructures with an atomic force microscope, Appl. Phys. Lett. 84 (2004) 1359-1361.
20. J. Mehlich, B.J. Ravoo, Click chemistry by microcontact printing on self-assembled monolayers: A structure-reactivity study by fluorescence microscopy, Org. Biomol. Chem. 9 (2011) 4108-4115.
21. G.J. Leggett, Scanning near-field photolithography-surface photochemistry with nanoscale spatial resolution, Chem. Soc. Rev. 35 (2006) 1150-1161.
22. A. Gölzhäuser, W. Eck, W. Geyer, V. Stadler, T. Weimann, P. Hinze, M. Grunze, Chemical nanolithography with electron beams, Adv. Mater. 13 (2001) 806-809.
23. P.M. Mendes, S. Jacke, K. Critchley, J. Plaza, Y. Chen, K. Nikitin, R.E. Palmer, J.A. Preece, S.D. Evans, D. Fitzmaurice, Gold nanoparticle patterning of silicon wafers using chemical e-beam lithography, Langmuir 20 (2004) 3766-3768.

24. P.M. Mendes, M. Belloni, M. Ashworth, C. Hardy, K. Nikitin, D. Fitzmaurice, K. Critchley, S.D. Evans, J.A. Preece, A novel example of X-ray-radiation-induced chemical reduction of an aromatic nitro-group-containing thin film on SiO_2 to an aromatic amine film, Chem. Phys. Chem. 4 (2003) 884-889.
25. W. Eck, V. Stadler, W. Geyer, M. Zharnikov, A. Gölzhäuser, M. Grunze, Generation of surface amino groups on aromatic self-assembled monolayers by low energy electron beams - a first step towards chemical lithography, Adv. Mater. 12 (2000) 805-808.
26. A. Biebricher, A. Paul, P. Tinnefeld, A. Gölzhäuser, M. Sauer, Controlled three-dimensional immobilization of biomolecules on chemically patterned surfaces, J. Biotech. 112 (2004) 97-107.
27. P. Iqbal, K. Critchley, D. Attwood, D. Tunnicliffe, S.D. Evans, J.A. Preece, Chemical manipulation by X-rays of functionalized thiolate self-assembled monolayers on Au, Langmuir 24 (2008) 13969-13976.
28. W. Geyer, V. Stadler, W. Eck, M. Zharnikov, A. Gölzhäuser, M. Grunze, Electron-induced crosslinking of aromatic self-assembled monolayers: negative resists for nanolithography, Appl. Phys. Lett. 75 (1999) 2401-2403.
29. S. Diegoli, P.M. Mendes, E.R. Baguley, S.J. Leigh, P. Iqbal, Y.R. Garcia Diaz, S. Begum, K. Critchley, G.D. Hammond, S.D. Evans, D. Attwood, I.P. Jones, J.A. Preece, pH-Dependent gold nanoparticle self-organization on functionalized Si/SiO_2 surfaces, J. Exp. Nano. Sci. 1 (2006) 333-353.
30. D.L. Feldheim, C.D. Keating, Self-assembly of single electron transistors and related devices, Chem. Soc. Rev. 27 (1998) 1-12.
31. T. Sato, D.G. Hasko, H. Ahmed, Nanoscale colloidal particles: monolayer organization and patterning, J. Vac. Sci. Tech. B. 15 (1997) 45-48.
32. W.P. McConnell, J.P. Novak, L.C. Brousseau, R.R. Fuierer, R.C. Tenent, D.L. Feldheim, Electronic and optical properties of chemically modified metal nanoparticles and molecularly bridged nanoparticle arrays, J. Phys. Chem. B 104 (2000) 8925-8930.
33. T. Liu, J. Tang, H. Zhao, Y. Deng, L. Jiang, Particle size effect of the DNA sensor amplified with gold nanoparticles, Langmuir 18 (2002) 5624-5626.
34. G. Frens, Controlled nucleation for regulation of particle-size in monodisperse gold suspensions, Nat. Phys. Sci. 241 (1973) 20-22.
35. J.F. Kang, A. Ulman, S. Liao, R. Jordan, G. Yang, G.Y. Liu, Self-assembled rigid monolayers of 4 '-substituted-4-mercaptobiphenyls on gold and silver surfaces, Langmuir 17 (2001) 95-106.
36. J.F. Moulder, W.F. Stickle, P.E. Sobol, K. Bomben, Handbook of X-ray Photoelectron Spectroscopy, Perkin-Elmer Corporation, 1992.
37. T. Tada, T. Kanayama, A.P.G. Robinson, R.E. Palmer, M.T. Allen, J.A. Preece, K.D.M. Harris, A triphenylene derivative as a novel negative/positive tone resist of 10 nanometer resolution, Microelectron. Eng. 53 (2000) 425-428.
38. K. Murata, D.F. Kyser, Monte-Carlo methods and microlithography simulation for electron and X-ray beams, Adv. Electron. Electron Phys. 69 (1987) 175-259.
39. N. Aizaki, Proximity effect dependence on substrate material, J. Vac. Sci. Tech. 16 (1979) 1726-1733.
40. Noy, A. Handbook of Molecular Force Spectroscopy Vol 1, Springer, 2008.
41. S. Hafizovic, D. Barrettino, T. Volden, J. Sedivy, K. Kirstein, O. Brand, A. Hierlemann, Single-chip mechatronic microsystem for surface imaging and force response studies, PNAS 101 (2004) 17011-17015.
42. O. Toikkanen, N. Doan, M. Erdmanis, H. Lipsanen, K. Kontturi, B. Parviz, Building molecular surface gradients with electron beam lithography, J. Micromech. Microeng. 21 (2011) 054025.
43. S. Lewis, D. Jeanmaire, V. Haynes, L. Piccirillo, Characterization of an ultra high aspect ratio electron beam resist for nanolithography, Nanotechnology 2010: Electronics, Devices, Fabrication, MEMS, Fludics & Computational, Vol 2, pp195-198, ISBN: 978-1-4398-3402-2.
44. D.C. Joy, 'Monte Carlo Modeling for Electron Microscopy and Microanalysis', pp. 33, Oxford University Press, (1995).
45. H. Niedrig, Electron backscattering from thin films, J. Appl. Phys. 53, (1982) R15.

List of figures

Figures

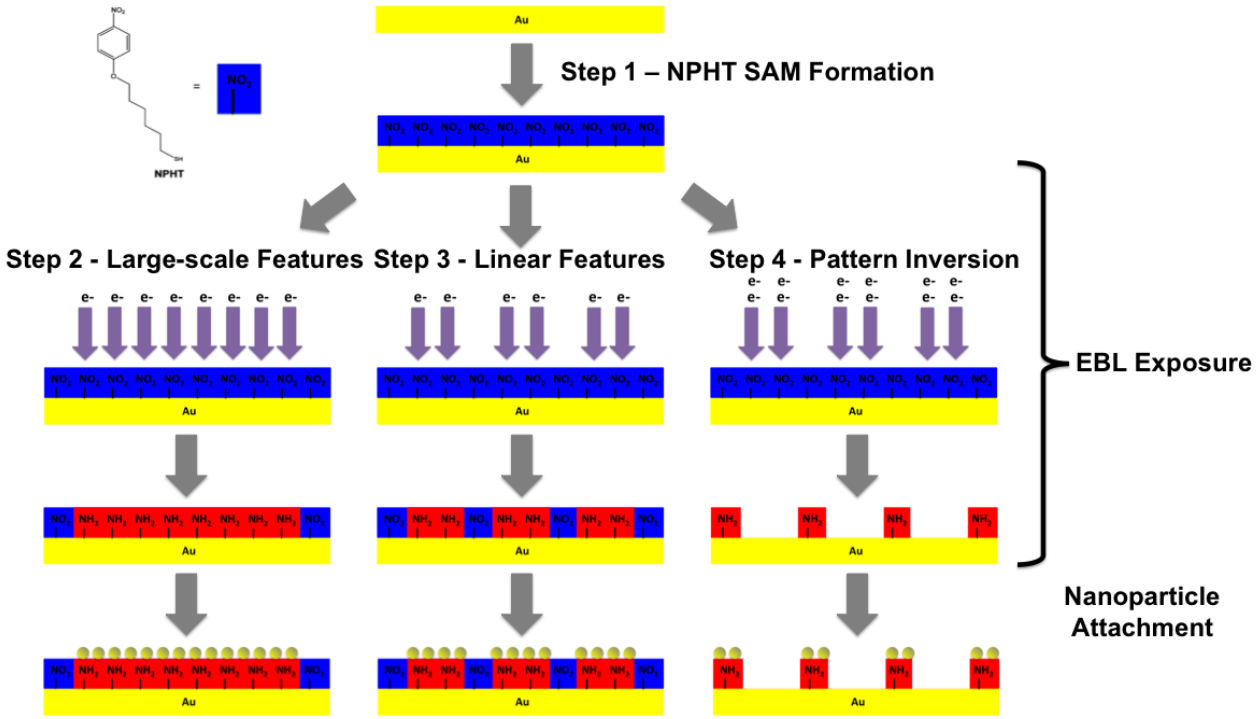

Figure 1. A schematic representation of the experimental steps carried out, (*step 1*) formation of the NO_2 terminated thiol SAMs on Au, (*step 2*) patterning of large scale features on NO_2 SAMs with EBL causing functional group conversion and attachment of negatively charged Au nanoparticles, (*step 3*) patterning of linear features with EBL and attachment of negatively charged Au nanoparticles and (*step 4*) high electron dose patterning with EBL causing pattern inversion and attachment of negatively charged Au nanoparticles.

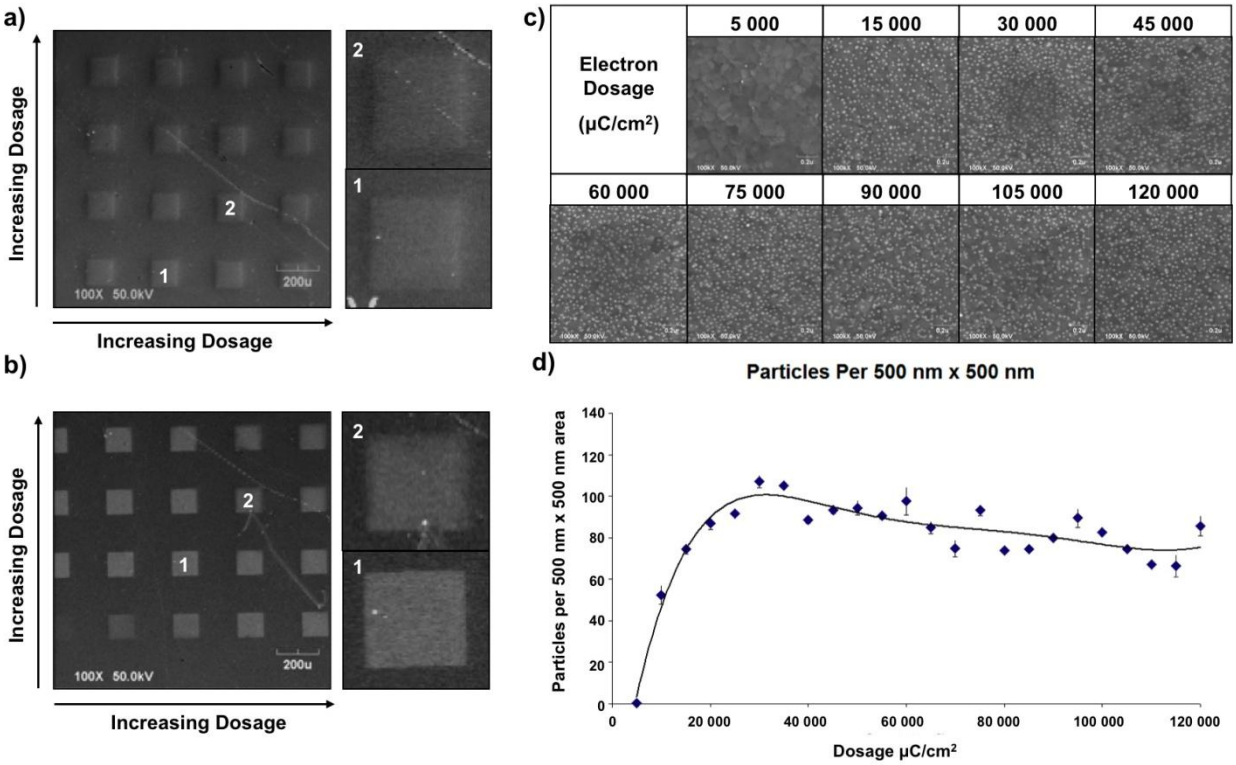

Figure 2. SEM Images of 120 µm x 120 µm square features after (*a*) EBL of NPHT SAM and (*b*) after subsequent immersion into Au-NPs at pH 4.5. Magnified regions 1 & 2 show little difference in contrast and resolution after EBL, but a large difference in contrast and resolution after immersion into Au-NP solution, (*c*) a selection of SEM images showing attachment of Au-NPs to NPHT SAM after exposure at increasing electron dosage and (*d*) graph summarising the density of Au-NP absorption as a function of electron dosage of NPHT SAM.

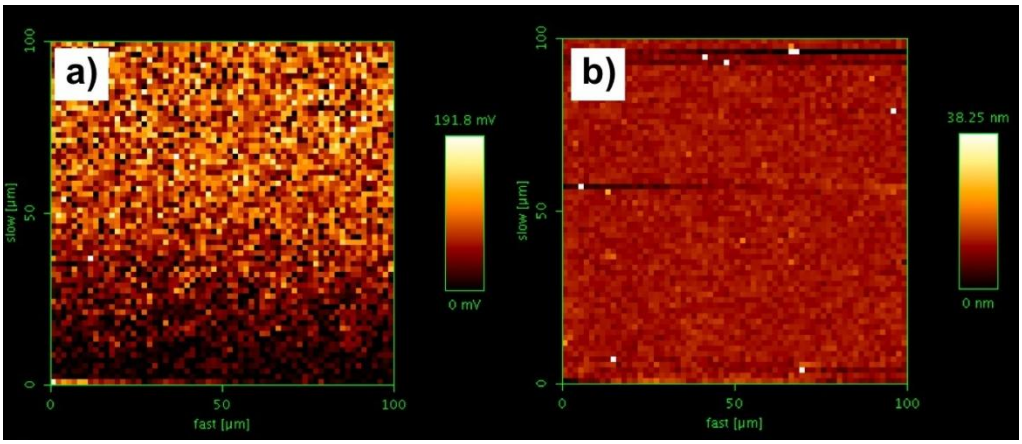

Figure 3. 100 µm x 100 µm (64 x 64 pixel) (*a*) adhesion force map and (*b*) height map of EBL exposed region before immersion in Au-NPs.

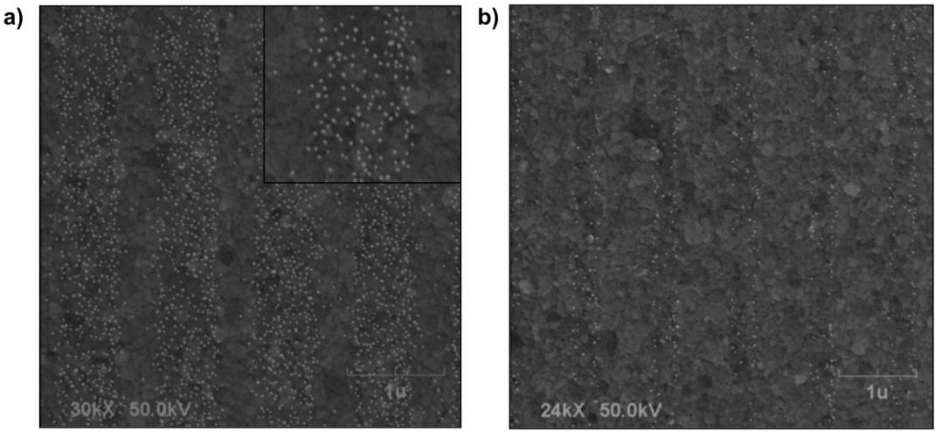

Figure 4 (*a*) SEM image showing attachment of Au-NPs on 400 nm wide type A features exposed at 40,000 µC/cm^2 and (*b*) SEM image showing attachment of Au-NPs only at the edge of 250 nm wide type B features exposed at 40,000 µC/cm^2.

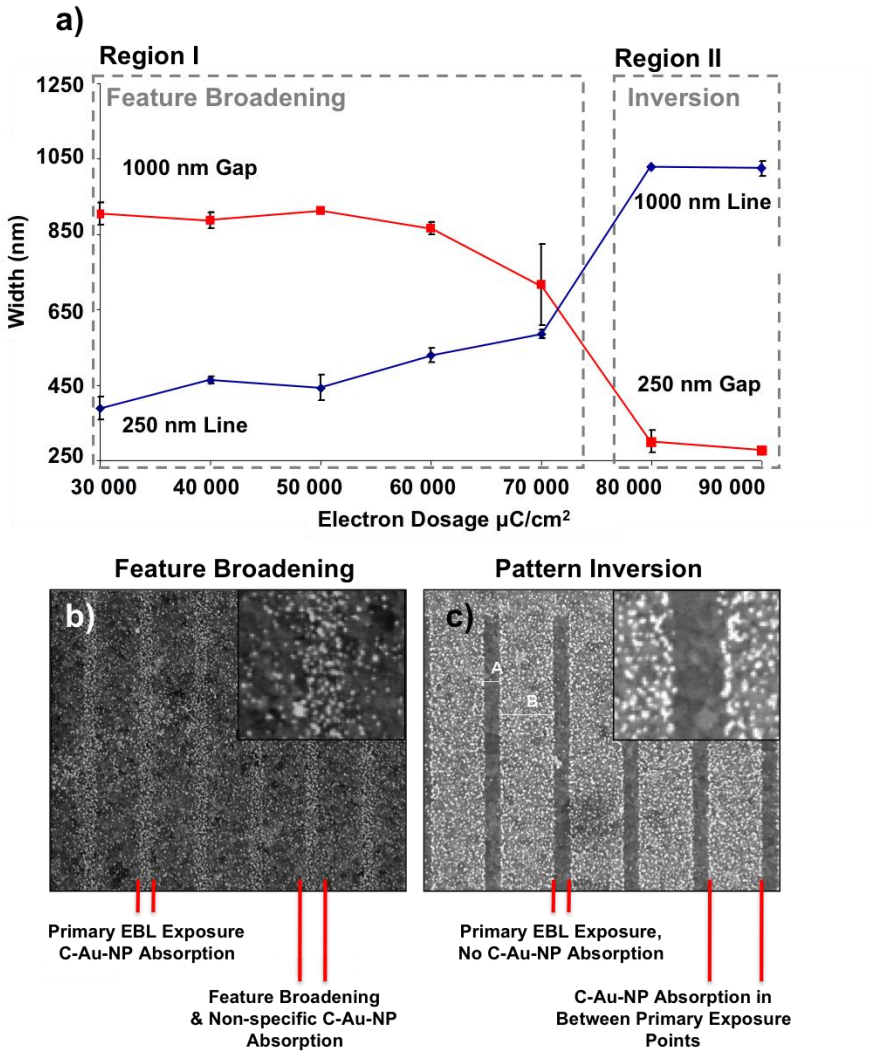

Figure 5. (*a*) graph showing the width of 250 nm lines (type C) of C-Au-NPs with 1000 nm separation, measured by AFM, plotted against the primary electron dosage of underlying SAM. Region I shows feature broadening with electron dose, while region II shows pattern inversion, (*b*) SEM image of 250 nm lines exposed at 45 000 µC/cm^2, with (type C) of Au nanoparticles deposited from a C-Au-NP solution and (*c*) SEM image of inverted features at 90 000 µC/cm^2, with no attachment of C-Au-NPs in regions of the primary electron dose of the SAM but attachment in the inter-feature gaps.

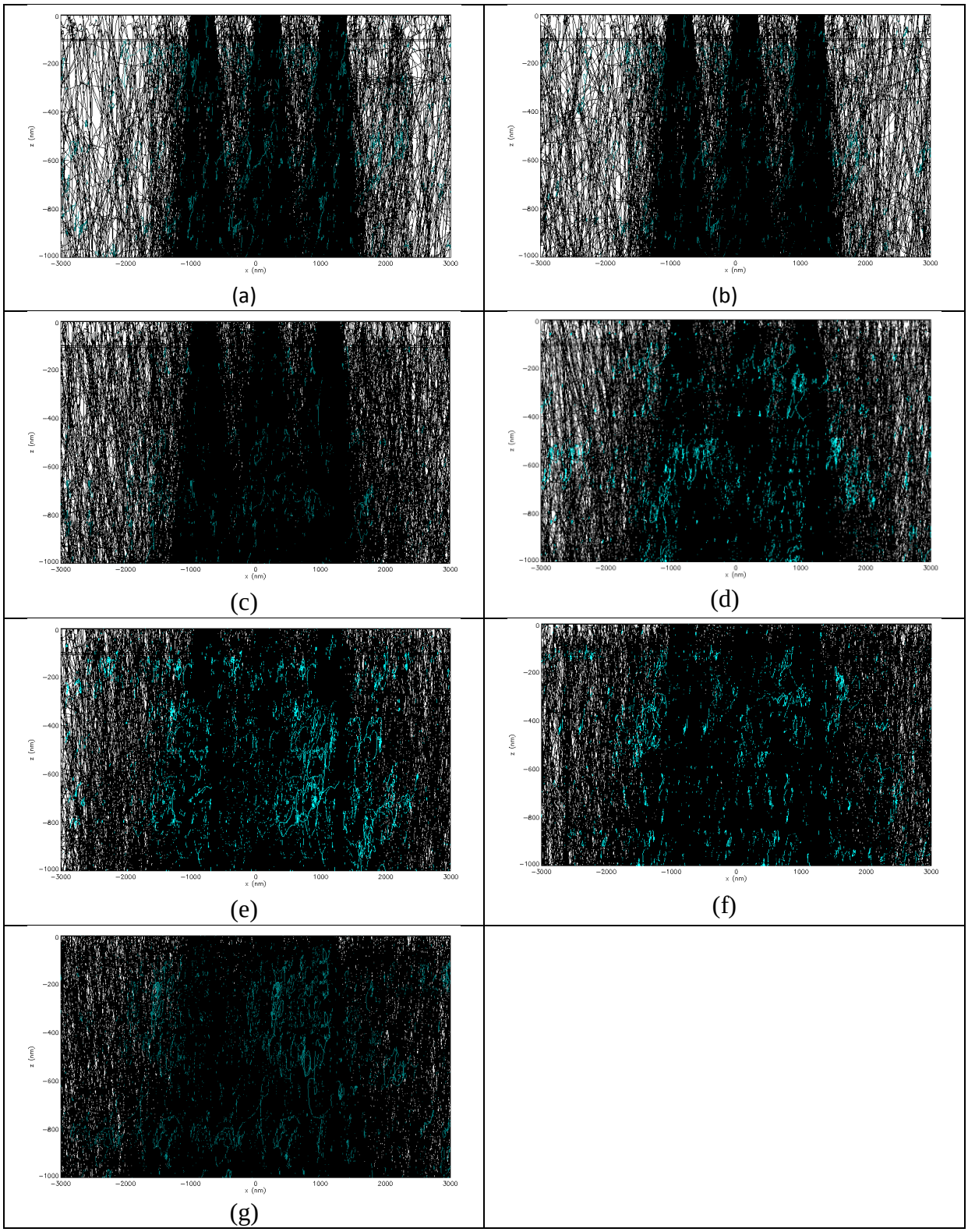

Figure 6. The internal electron scattering interactions inside the sample at a dose of (a) 30,000 μC/cm^2, (b) 40,000 μC/cm^2, (c) 50,000 μC/cm^2, (d) 60,000 μC/cm^2, (e) 70,000 μC/cm^2, (f) 80,000 μC/cm^2, and (g) 90,000 μC/cm^2; image dimensions 6 μm x 1 μm.

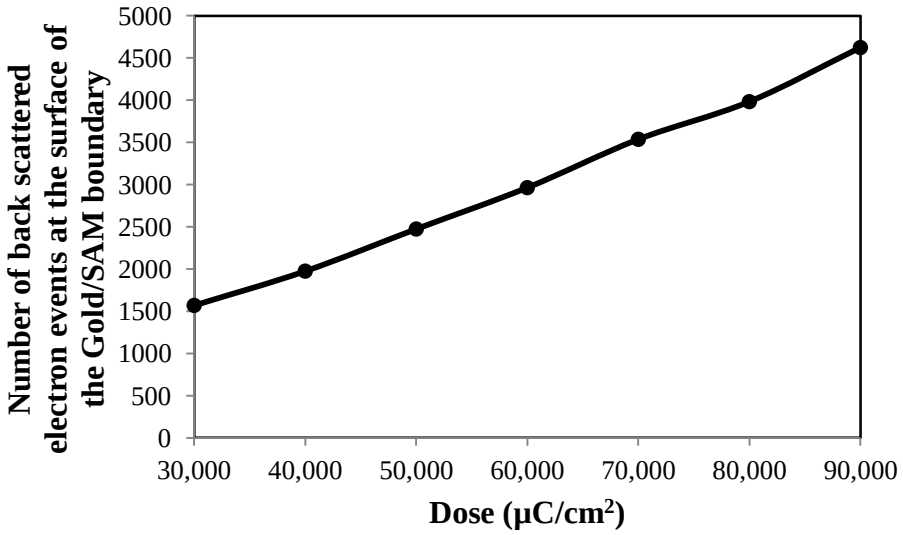

Figure 7. The number of back scattered electrons incident into the SAM from the Au layer.